Engineering Fracture Mechanics 207 (2019) 203–221

Contents lists available at ScienceDirect

Engineering Fracture Mechanics

journal homepage: www.elsevier.com/locate/engfracmech

Fracture behavior of carbon fiber reinforced polymer composites: An optical study of loading rate effects

Chengyun Miao, Hareesh V. Tippur*

Department of Mechanical Engineering, Auburn University, AL 36849, USA

ARTICLE INFO

Keywords:
Carbon fiber reinforced plastics
Loading rate effects
Dynamic fracture
Crack growth behavior
Digital Gradient Sensing

ABSTRACT

Crack initiation and growth in single-edge notched unidirectional T800s/3900-2 CFRP laminates are studied under stress wave and quasi-static loading conditions. An optical technique called reflection-mode Digital Gradient Sensing is also extended to study fracture mechanics of CFRP by using it in conjunction with ultrahigh-speed photography to perform full-field measurement of crack-tip deformations in the pre- and post-crack initiation regimes. DGS is capable of measuring two orthogonal surface slopes in the crack-tip vicinity as angular deflection of light rays. A method for extracting crack-tip parameters – the instantaneous crack speed and stress intensity factor (SIF) histories – associated with the stationary and propagating cracks using measured surface slopes is presented. The effect of fiber orientation in the range 0°–60° relative to the initial notch and two loading rates are investigated. Nominally mode-I fracture occurs when the fiber orientation is 0° whereas mixed-mode fractures ensue in others. Besides crack initiation occurrence at higher loads as fiber orientation increases, the SIF histories imply strong fiber bridging at low fiber orientations under quasi-static conditions. Furthermore, this CFRP shows significant loading rate dependence during crack growth. Unlike stress wave loading conditions, an increasing crack growth resistance immediately after crack initiation is seen under quasi-static conditions.

1. Introduction

Carbon fiber reinforced polymer (CFRP) composites have become materials of choice in many aerospace and automotive structures [1–3]. The high strength, high stiffness, impact resistant and lightweight characteristics have made them very popular in these and other applications. However, fiber reinforced plastics (FRP) in general are comprised of weak matrix-fiber interfaces and hence prone to disbonds and crack-like defects during fabrication or service. As a result, crack initiation and growth originated from such defects under different loading conditions and loading rates is a distinct possibility. Hence, it is critical that relevant engineering parameters in general and failure characteristics in particular are fully quantified by understanding the mechanisms that control the fracture behaviors of CFRP under different loading rates.

Several researchers have studied the fracture behaviors of polymer composites subjected to quasi-static and dynamic (impact) loads [4–6]. Those studies are often based on globally measured mechanical quantities (e.g., far-field loads and/or deflections) and fractography of the fractured surfaces. May [7] has reviewed different testing geometries to measure rate-dependent mode I fracture toughness of composites to conclude that wedge-loaded Double Cantilever Beam (DCB) is suitable for measuring the mode I fracture toughness. Beckermann [8] and Seyhan [9] conducted DCB tests and End Notched Flexure (ENF) tests to study mode I and mode II

* Corresponding author. McWane Endowed Chair Professor. Tel.: +1 334 844 3327.
E-mail address: tippuhv@auburn.edu (H.V. Tippur).

https://doi.org/10.1016/j.engfracmech.2018.12.035
Received 7 September 2018; Received in revised form 23 December 2018; Accepted 29 December 2018
Available online 31 December 2018
0013-7944/

fracture toughness of different composites (unidirectional carbon/epoxy composite and glass fiber/carbon nanotube reinforced composite). Their results were based on measurement of loads imposed in the far-field. Shukla et al. [10,11] developed strain-gage methods to measure strains and hence fracture parameters in glass fiber reinforced epoxy laminate $[0_2/90]_{2s}$.

Full-field optical methods have distinct advantages relative to global load or displacement measurement techniques as they allow quantitative visualization of mechanical quantities in the entire region-of-interest (ROI) via non-contact means and hence are preferable to study fracture mechanics of various materials including fiber reinforced composites. Freire et al. investigated the stress state in glass fiber reinforced polyester laminated composites using reflection photoelasticity [12]. Shukla and Khanna also studied crack growth in different unidirectional low-volume fraction model composites reinforced with glass fibers and metal fibers photoelastically and have noted that fiber bridges reduced the stress intensification and crack velocity [13]. Liu et al. extended the optical method of Coherent Gradient Sensing (CGS) [14] to study static and dynamic fracture behaviors of graphite/epoxy unidirectional fiber-reinforced composites (IM7/8551-7) [15,16]. Hatta et al. applied electronic speckle pattern interferometry (ESPI) to evaluate fracture process in cross-ply carbon fiber reinforced composite laminates and concluded that ESPI was effective in identifying small-scale delaminations [17]. In recent years, due to advances in digital recording technologies and image processing algorithms, Digital Image Correlation (DIC) methods have become popular for measuring full-filed surface deformations [18–26]. Mekky and Nicholson [19] explored crack opening displacement extraction in ceramic/metal composite laminates using DIC. Kirugulige et al. [21,20] were the first to demonstrate DIC in conjunction with ultrahigh-speed photography to study dynamic fracture of polymers and structural foams. Lee et al. [22,23] extended the idea to investigate crack growth in unidirectional CFRP composites (T800/3900-2) coupons subjected to dynamic impact. More recently, Bedsole et al. [24] investigated interlaminar vs. intralaminar dynamic fracture characteristics of unidirectional CFRP using DIC. 3D-DIC has been adopted by Mallon et al. [25] to study fracture behavior of pre-stressed orthotropic woven glass fiber-reinforced composites under out-of-plane shock tube loading up to crack initiation. Hoffmann et al. [26] applied DIC to study strain field around crack tip in composite laminates (unidirectional carbon fiber reinforced prepreg stacked with $[(90,0)_8,90]_s$ lay-up) under quasi-static and high-rate loading conditions and noted that the strain-energy release rate of a composite laminate under high-rate loading was lower than its quasi-static counterpart.

Understanding the dynamic crack growth in fiber reinforced composites continues to be rather challenging from the perspective of full-field measurement of mechanical fields. In addition to the obvious issues of lack of optical transparency or the need for specimen surface preparation required to implement legacy optical methods, the abundance of weak fiber-matrix interfaces and large directional stiffness result in relatively high crack speeds (500–1000 m/s) accompanied by small deformations (a few micrometers) pose challenges to experimental investigations. Difficulty of identifying crack-tip location precisely for accurate evaluation of fracture parameters is among the major issues for vision-based investigations [22] of in-plane, non-singular displacements. In this context, modified vision-based techniques coupled with advanced ultrahigh-speed imaging technology could alleviate such problems. Recently, a full-field optical method called Digital Gradient Sensing (DGS) has been introduced for measuring two orthogonal angular deflections of light rays caused by stresses in transparent materials [27] and out-of-plane deformations of reflective solids [28]. By coupling the reflection-mode DGS or, r-DGS, with a 2D least-squares integration scheme, surface topography of thin structures with sub-micron resolution over relatively large ROI ($\sim$75 mm dia.) of composite plates have been achieved [29,30]. Attempts to further increase the measurement sensitivity of these DGS methods have been reported as well [31]. Considering the recent success of Sundaram and Tippur to study dynamic fracture of extremely brittle materials such as float glass [32–34] using transmission-mode DGS where crack speeds are very high and deformations are very small, examining the feasibility of r-DGS to similar challenging problem in opaque structural materials such as CFRP is an obvious next step. A successful demonstration could not only provide a complementary experimental tool for the FRP community but offer additional insight into the fracture characteristics of these popular structural materials.

In the following, the method of r-DGS is briefly introduced first. Details regarding the crack-tip fields for edge cracked composite specimens subjected to dynamic and quasi-static loads measured by r-DGS are discussed next. This is followed by an outline of fracture parameters (crack growth, stress intensity factors and energy release rate) extraction from the optical measurements at different loading rates. Finally, results pertaining to fracture characteristics under different loading rates are discussed and major conclusions are drawn.

2. Optical method

A schematic of the optical setup for reflection-mode Digital Gradient Sensing (r-DGS) is shown in Fig. 1. A camera is used to record random speckles/texture on a target plane via the specular specimen surface. Typically, this is achieved by placing the specimen plane and the target plane parallel to each other and a 50/50 beam splitter at 45° relative to both. The target plate is sprayed with black and white paints to create random speckles. To facilitate recording of the speckles via the specimen surface, the specimen is made reflective by vapor deposition with an aluminum film [35].

Fig. 2 explains the working principle of r-DGS. For simplicity, the angular deflections of light rays in the x-z plane are shown and similar arguments can be extended to the y-z plane as well. When the specimen is in the undeformed state, the intensity at a point P on the target plate is recorded by one of the pixels of the camera sensor through point O on the specimen surface. The gray scales recorded at this time-instant or load-state by all the pixels serve as the reference image. After the specimen suffers out-of-plane deformation, the intensity at a neighboring point Q on the target plate is recorded by the same pixel of the sensor through the same point O on the specimen surface. The corresponding gray scales in the deformed state of the specimen are recorded next by the camera sensor. The local displacement δ_x in the x-z plane can be obtained by performing a 2D digital image correlation (DIC) of the reference and deformed images. The angular deflection of a generic light ray ϕ_x is explained as follows. The ray OP makes an angle ϕ_x

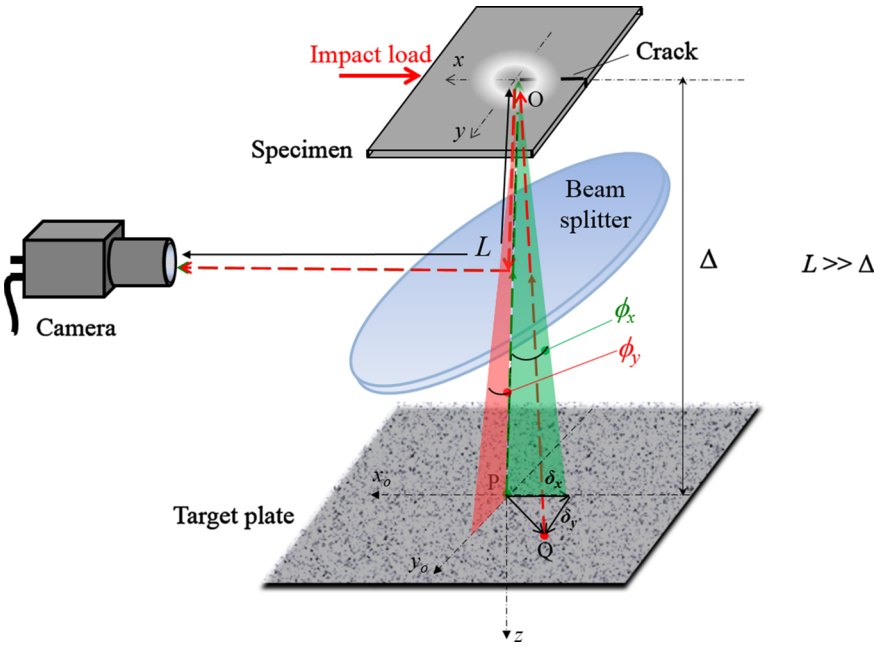

Fig. 1. Schematic of experimental setup for reflection DGS (r-DGS).

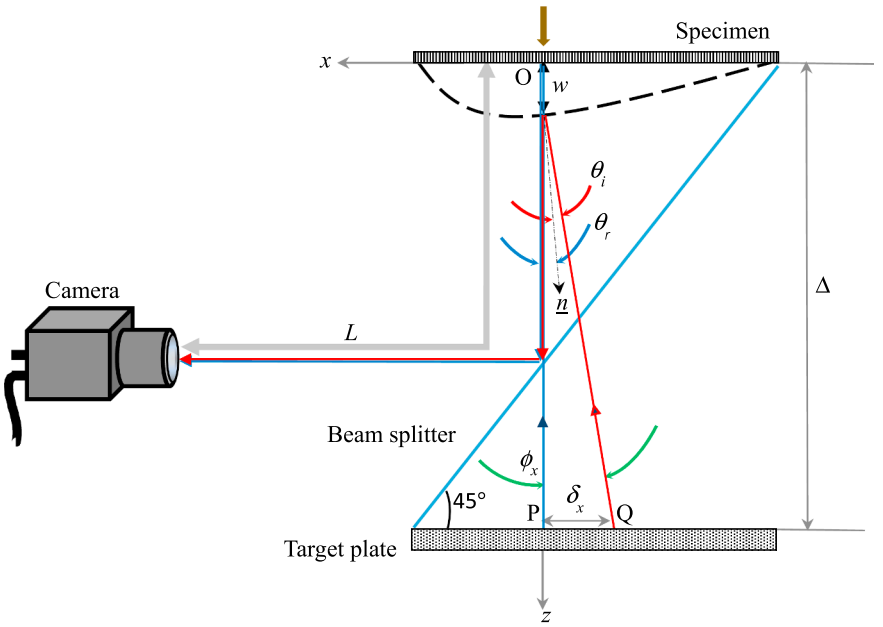

Fig. 2. Working principle of r-DGS [29].

with OQ and $\phi_x = \theta_i + \theta_r$ where θ_i and θ_r $(=\theta_i)$ are the incident and reflected angles relative to the local normal to the specimen. Similar arguments hold for speckle displacements in the *y*-*z* plane and the corresponding angular deflection ϕ_y. The two orthogonal surface slopes can then be expressed as $\frac{\partial w}{\partial x; y} = \frac{1}{2}\tan(\phi_{x;y})$. By invoking the small angle approximation, the governing equations for r-DGS become [28]:

$$\frac{\partial w}{\partial x; y} = \frac{1}{2}\tan(\phi_{x;y}) \approx \frac{1}{2}(\phi_{x;y}) \approx \frac{1}{2}\left(\frac{\delta_{x;y}}{\Delta}\right) \tag{1}$$

where Δ is the distance between the specimen and target planes.

It is important to note that the coordinates of the specimen plane are used in the above governing equations. However, the camera is focused on the target plane for recording the speckles. Therefore, by incorporating the pin-hole camera approximation the

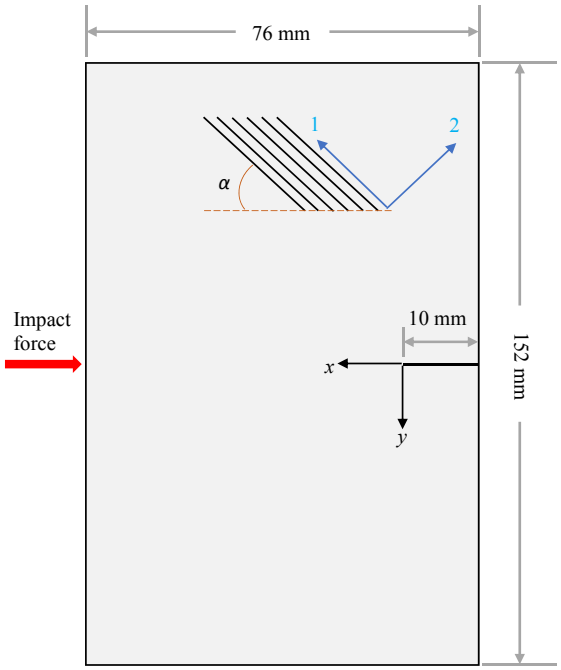

Fig. 3. Specimen configuration.

coordinates of the target can be transferred to the specimen as $(x; y) = \frac{L}{L+\Delta}(x_0; y_0)$ where $(x; y)$ and $(x_0; y_0)$ represent the coordinates of the specimen and target planes, respectively, and L is the distance between the specimen and camera [27].

3. Dynamic fracture

Fracture behavior of CFRP plates made of T800s/3900-2 unidirectional laminate with a $[0_{36}]$ lay-up (Toray Composite Materials America, Inc.) were studied first. The specimens were cut into 152 mm × 76 mm × 6.8 mm plates of five different fiber orientations, $\alpha = 0^\circ, 15^\circ, 30^\circ, 45^\circ$ and 60° with respect to the initial edge crack direction, as depicted in Fig. 3. The elastic properties of T800s/3900-2 unidirectional laminate are listed in Table 1 [36] where subscripts 1 and 2 represent directions along and normal to the fiber direction, respectively, and subscript 3 represents the out-of-plane direction. For specimens with different fiber orientations, elastic moduli and Poisson's ratios, corresponding to the global coordinate system shown in Fig. 3, were computed by rotational transformations and are listed in Table 2. The so-called degree-of-anisotropy, $\frac{E_{xx}}{E_{yy}}$, for different specimens are also listed in Table 2. For each specimen, a 10 mm long horizontal pre-notch was cut at the middle of the long edge using a 300 μm thick diamond saw and then sharpened using a steel razor blade. The impact load was also imposed at the middle of the edge opposite to the cracked edge. That is, when $\alpha = 0^\circ$ nominally mode-I fracture conditions occur whereas mixed-mode (mode-I + II) conditions arise for all other non-zero angles. One of the two 152 mm × 76 mm faces of each specimen was made reflective by using the aluminum film transfer technique to implement r-DGS.

The schematic of the experimental setup used is shown in Fig. 4. A modified Hopkinson pressure bar, or simply a 'long-bar', was used for loading the edge-cracked composite specimens. The long-bar was a 1.83 m steel rod of 25.4 mm diameter with a polished wedge-shaped tip for impacting an unconstrained CFRP plate on the edge opposite to the cracked edge. A 305 mm long, 25.4 mm diameter steel striker placed in the barrel of a gas-gun was co-axially aligned with the long-bar at the start of the experiment. The striker was launched towards the long-bar at a velocity of approx. 6 m/s during tests. A close-up view of the optical arrangement is also shown in Fig. 4. Initially, the long-bar tip was kept in contact with the specimen. The specimen was positioned on the platform using a rectangular soft putty strip to prevent direct contact with the platform. To achieve symmetry in terms of acoustic impedance relative to the loading axis, another putty strip was pressed onto the top edge of the specimen. The lower putty strip isolated the specimen from the support to create an approximately 'free surface' condition away from the loading point. A beam splitter and the

Table 1
Material properties of T800s/3900-2 unidirectional laminate [36].

E_1 (GPa)	E_2 (GPa)	G_{12} (GPa)	ν_{12}	ν_{13}	ν_{23}	Density
152.0	8.0	4.0	0.34	0.34	0.45	1600 kg/m^3

Table 2
Material properties of specimens with different α.

	$\alpha = 0^\circ$	$\alpha = 15^\circ$	$\alpha = 30^\circ$	$\alpha = 45^\circ$	$\alpha = 60^\circ$
E_{xx} (GPa)	152.0	46.2	17.4	10.6	8.6
E_{yy} (GPa)	8.0	8.1	8.6	10.6	17.4
G_{xy} (GPa)	4.0	4.5	6.1	7.5	6.1
ν_{xy}	0.34	0.43	0.41	0.33	0.20
E_{xx}/E_{yy}	19.0	5.7	2.0	1.0	0.5

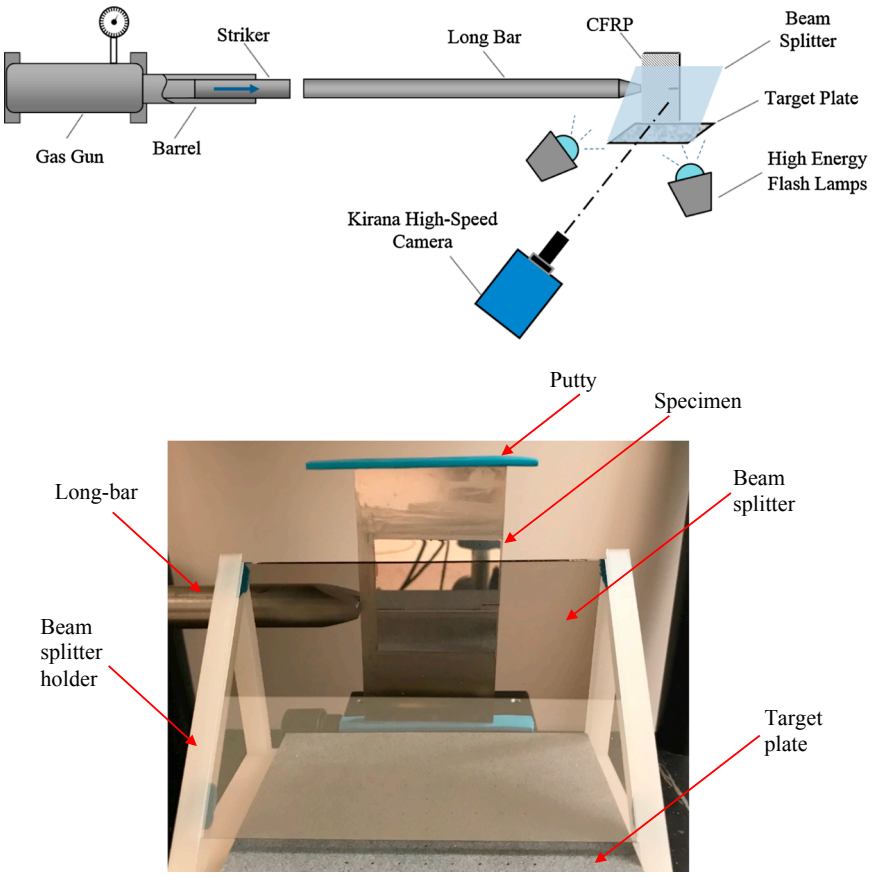

Fig. 4. Schematic (top) and close-up photograph (bottom) of the experimental setup used to study dynamic fracture behavior of CFRP.

speckle target plate were placed in a specially designed 45° holder so that the camera could be focused on the speckles through the beam splitter via the reflective specimen surface. The speckle images were photographed by a Kirana-05 M ultrahigh-speed digital camera, a single sensor camera capable of recording 180 10-bit gray scale images at a maximum rate of 5 million frames per second and spatial resolution of 924 × 768 pixels per image. The speckles on the target plate were illuminated using a pair of Cordin-659 high energy flash lamps.

A Nikon 70–300 mm focal length zoom lens with an adjustable bellows was used with the camera to record the speckle images from a long distance. An optimum sensor exposure and focus were achieved by stopping down the lens aperture to $F^{\#}11$ after focusing. The distance between the specimen and the lens plane (L) was ~780 mm and the one between the specimen mid-plane and the target plane (Δ) was ~70 mm. With these settings, the camera recorded information from a rectangular region of approximately 40 mm × 35 mm on the specimen plane in the vicinity of the pre-notch tip as the region-of-interest (ROI). When the long-bar was impacted by the striker, a compressive stress wave propagated the entire length of the bar. Also, a trigger pulse was generated at the moment of impact to start recording the speckle images by the camera with a prescribed delay. A total of 180 images, some in the undeformed state and others in the deformed state of the specimen, were recorded at 500,000 frames per second (inter frame period 2 μs). One image just before the start of deformation was selected as the reference image. Subsequent images corresponding to the deformed state were correlated with the reference image using ARAMIS® image analysis software. During analysis, a sub-image size of 30 × 30 pixels with 25 pixels overlap was used to extract the local displacements $\delta_{x,y}$ in the ROI. It should be noted that 1 pixel in the recorded image is corresponded to 45.68 μm. The lower limit of measurable in-plane displacements using DIC being 1–2% of this

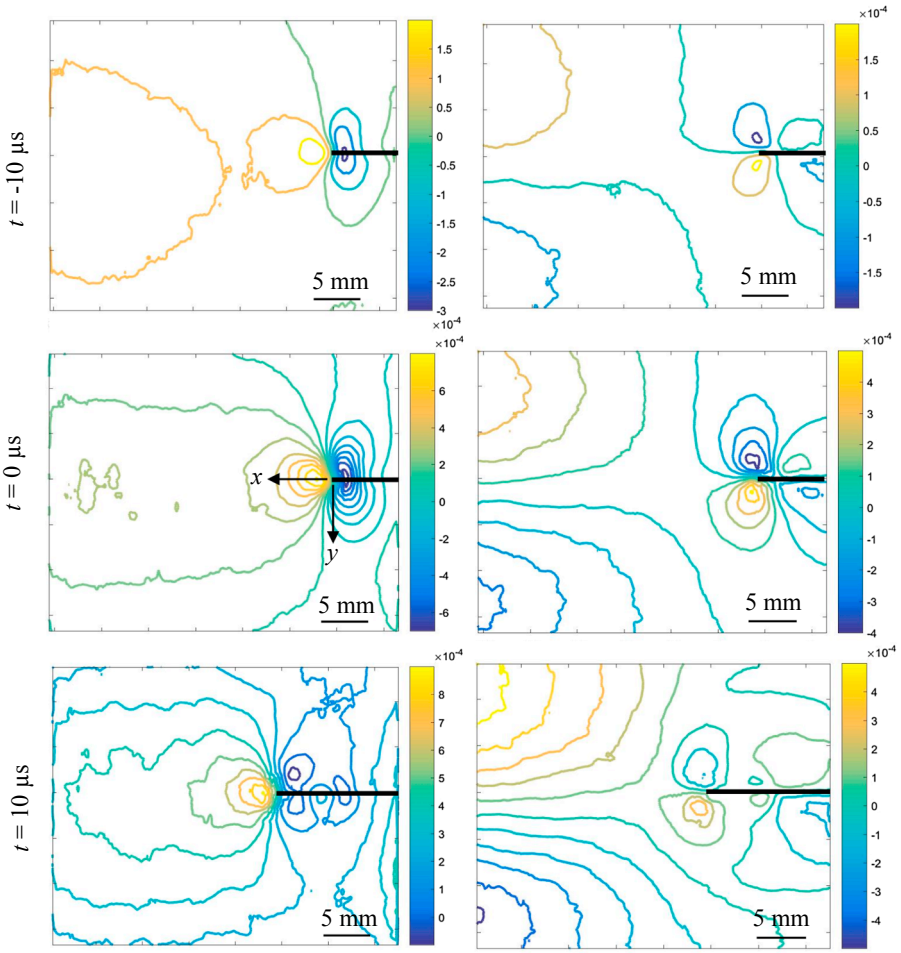

Fig. 5. Measured surface slopes $w_{,x}$ (left column) and $w_{,y}$ (right column) contours for CFRP of mode-I dynamic fracture. Contour increment = 1×10^{-4} rad. Black strips highlight the crack.

scaling factor, under ideal conditions the smallest measurable angular deflection is $\sim \pm 13 \times 10^{-6}$ rad. Also, the effects of sub-image size and step size chosen for analysis are reported in Ref. [30]. The displacement fields were then used to compute the two orthogonal surface slopes, $\frac{\partial w}{\partial x;y}$.

Measured surface slopes of $\frac{\partial w}{\partial x;y}$ around a dynamically loaded mode-I crack for $\alpha = 0^\circ$ are shown in Fig. 5 at a few select time instants. In these plots, $t = 0$ μs corresponds to crack initiation at the original notch-tip. It can be observed that, due to the symmetric nature of mode-I fracture, the crack propagates along a horizontal path (from right to left in these images) and hence the contours are generally symmetric in shape relative to the initial crack. The increasing size of $\frac{\partial w}{\partial x;y}$ contours during propagation qualitatively indicates an increase in stress intensity factors during crack propagation. It can be observed that contours of $\frac{\partial w}{\partial x}$ are rather well-defined when compared to those for $\frac{\partial w}{\partial y}$, especially after crack initiation. This is because the fiber orientation being along the horizontal direction, $\frac{\partial w}{\partial x}$ contours are affected to a lesser extent by the fibers when compared with the $\frac{\partial w}{\partial y}$ counterparts. The contours near the left-hand edge in these plots are attributed to the concentration of deformations due to the impact load imposed on that edge (outside the ROI).

For completeness, the contours of out-of-plane displacements ($w(x, y)$) computed by 2D integration of slope data from r-DGS in conjunction with Higher-order Finite-difference-based Least-squares Integration (HFLI) algorithm [29] are plotted in Fig. 6. Based on the smallest measurable angular deflection, the quantifiable out-of-plane displacement from the least-squares integration scheme is well below ± 0.2 µm. The singular crack-tip deformations (negative values) before crack initiation and during crack growth are clearly evident. A noticeable concentration of positive $w(x, y)$ along the left hand edge is again attributed to the impact loading on the coupon.

The measured surface slopes of $\frac{\partial w}{\partial x}$ around the dynamically loaded cracks for $\alpha = 15^\circ, 30^\circ, 45^\circ, 60^\circ$ are shown in Fig. 7 at a few select time instants. It should be noted that, all the contours depicted in Fig. 7(b) are plotted in the coordinates (x, y). The mixed-mode fracture behaviors can be readily observed here due to the fiber orientations being not along the loading direction namely the

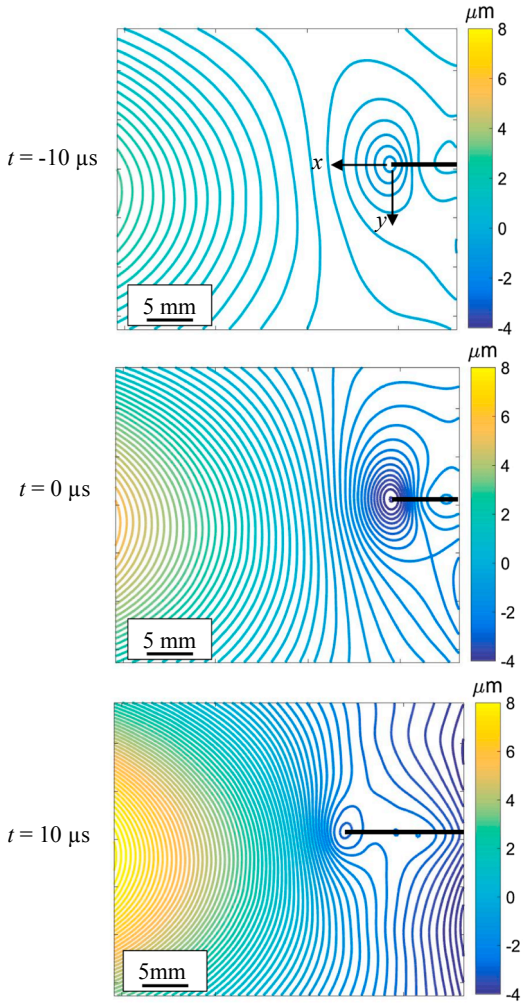

Fig. 6. Contours of out-of-plane displacements ($w(x, y)$) (0.2 µm intervals) for CFRP during mode-I dynamic fracture at a few select time instants before and after crack initiation ($t = 0$). Black strips highlight the crack. Concentration of (+) out-of-plane displacements at the left hand edge is due to impact loading whereas singularity of w-field around the crack tip (−) is due to the discontinuity.

-x-axis. Fig. 7(a)–(d) correspond to $\frac{\partial w}{\partial x}$ of each specimen at $t = 0\ \mu s$ or just before crack initiation; it can be observed in these plots that these contours generally lack symmetry relative to the initial crack orientation and become more tilted as the fiber orientation increases. Fig. 7(e)–(h) correspond to $\frac{\partial w}{\partial x}$ of each specimen at $t = 20\,\mu s$, or when the cracks have propagated for 20 µs after crack initiation in each case. The dominant contours are at the current crack-tip whereas those at the original notch-tip represent residual/unrecovered deformations. The dotted lines indicate the crack path after initiation and solid lines represent the initial crack direction in these plots. It can be observed that the crack propagation occurs along the fiber direction as expected although they are subjected to identical geometrically symmetric impact loading. Furthermore, the specimen with $\alpha = 15^{\circ}$ has the longest crack growth at $t = 20\,\mu s$, and the amount of crack growth is lower with increasing angles of fiber orientation relative to loading direction.

Again, for completeness, the contours of out-of-plane displacements ($w(x, y)$), corresponding to the plots in Fig. 7, computed using the 2D least-squares integration, are plotted in Fig. 8. Concentrations of singular crack-tip deformations (negative) before crack initiation and during crack growth are clearly evident. Evidently, higher concentration of $w(x, y)$ at crack initiation relative to the one during propagation qualitatively suggests a drop in the stress intensification during dynamic growth. Additionally, it can be observed in Fig. 8(a)–(d) that these out-of-plane displacements are somewhat more inclined as the fiber orientation increases, same as the phenomenon observed in Fig. 7(a)–(d).

The crack growth histories during dynamic crack growth are plotted in Fig. 9(a). Quadratic Bezier curves [37] with 0.5 as the control point were fitted to the instantaneous crack length (symbols) data resulting in smoothed crack growth histories (solid lines) shown in Fig. 9(a). The crack speed histories are plotted in Fig. 9(b). These generally show that after crack initiation the crack accelerates to a steady-state condition within 2–3 time steps. The averaged crack speed during steady state growth part was calculated in each case. Evidently, for $\alpha = 0^{\circ}$, 15° and 30° cases the crack growth histories bunch up in a narrow range. That is, their average crack speeds are between 690 and 720 m/s. However, for $\alpha = 45^{\circ}$, a significant drop in speed to ~518 m/s. For $\alpha = 60^{\circ}$, the

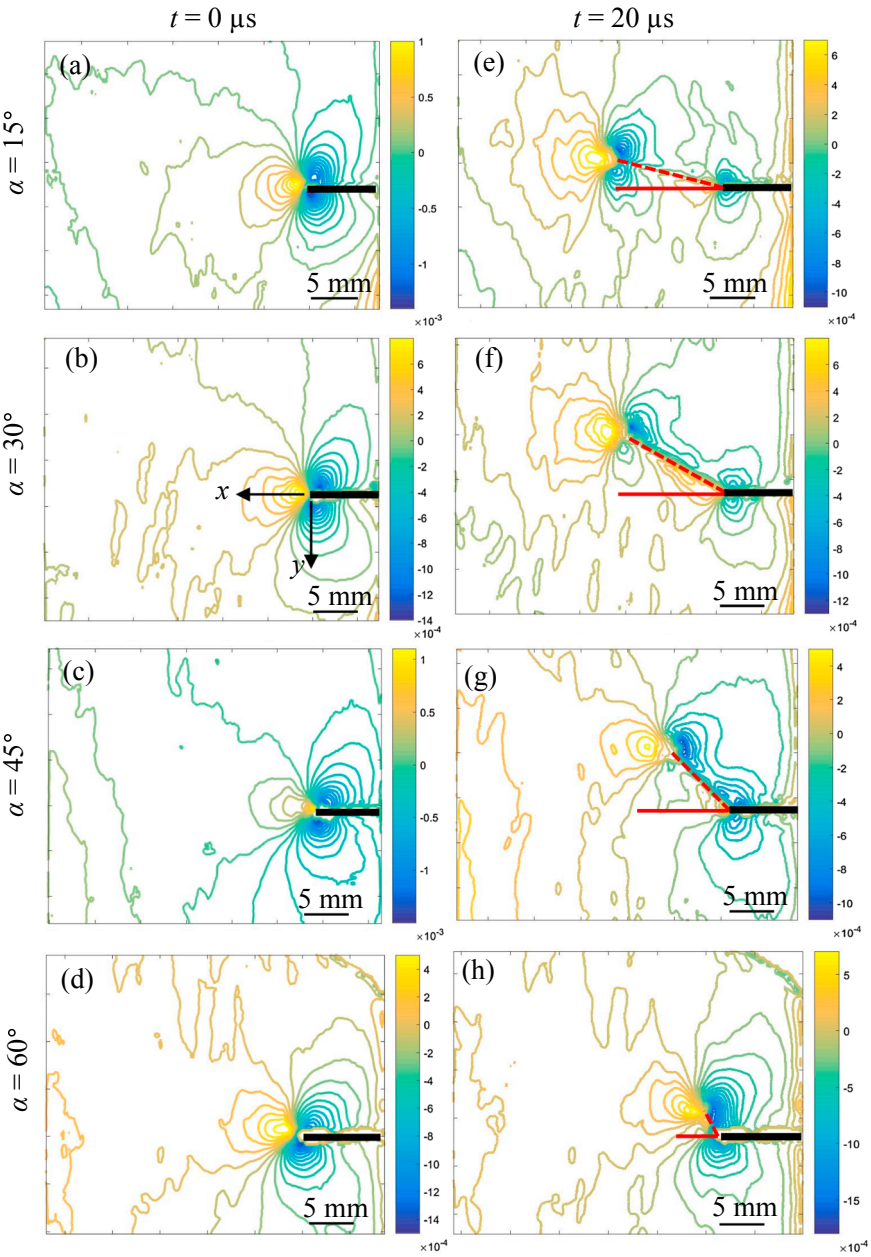

Fig. 7. Measured surface slopes $w_{,x}$ contours for CFRP of mixed-mode dynamic fracture. Contour increments = 1×10^{-4} rad. (Black strips are overlaid to highlight the crack; broken red line suggests kinked crack growth path.) (For interpretation of the references to colour in this figure legend, the reader is referred to the web version of this article.)

crack growth occurred at the lowest speed of 200 m/s following initiation and decelerated to < 100 m/s at later stages of growth.

4. Quasi-Static fracture

To study the loading rate effect on fracture behaviors of CFRP, quasi-static symmetric 3-point bending experiments were performed on edge notched CFRP coupons using r-DGS to measure deformations. Rectangular CFRP specimens of dimensions 152 mm × 56 mm × 6.8 mm with an initial crack of length 10 mm were used. As in the dynamic experiments, the specimens had different fiber orientations, $\alpha = 0^\circ$, 15°, 30° and 45°, with respect to the initial crack direction, as shown in Fig. 10(a). (The load required to initiate the crack in the $\alpha = 60^\circ$ case exceeded the limit of the loading device and hence static fracture of that configuration was not studied.) The specimens supported on two anvils (span 127 mm) were loaded using an Instron 4465 universal testing machine operating in displacement-control mode (cross-head speed = 0.007 mm/s). One of the two 152 mm × 56 mm faces of each

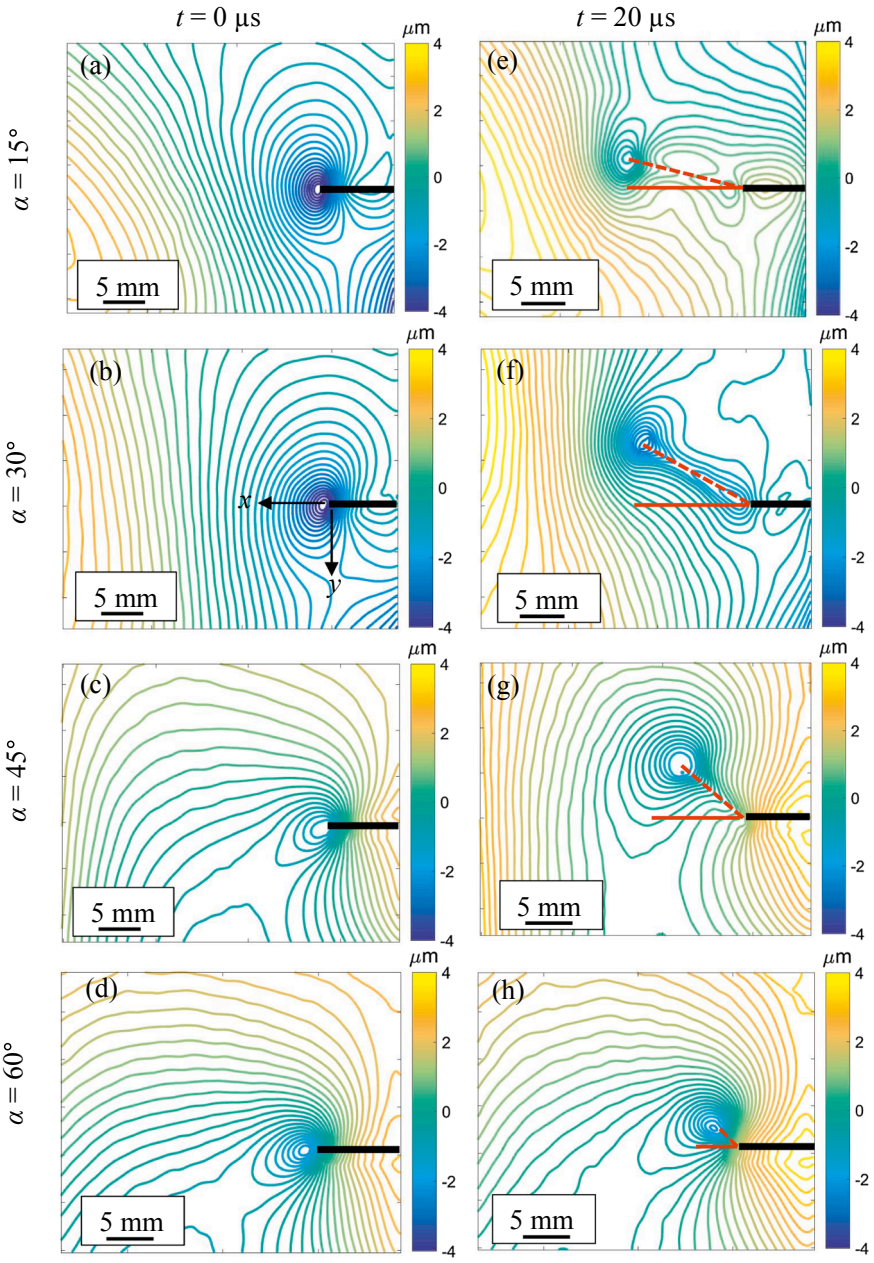

Fig. 8. Contours of out-of-plane displacements ($w(x, y)$) (0.2 μm intervals) for CFRP during mixed-mode dynamic fracture at a few select time instants. (Black strips are overlaid to highlight the crack; broken red line suggests kinked crack growth path.) Concentration of (+) out-of-plane displacements at the left hand edge is due to impact loading whereas singularity of w-field around the crack tip (−) is due to the discontinuity. (For interpretation of the references to colour in this figure legend, the reader is referred to the web version of this article.)

specimen was made reflective using the aluminum film transfer technique to implement r-DGS. The schematic of the static experimental setup is shown in Fig. 10(b). A beam splitter and the speckle target plate were placed in a 45° holder so that the camera could be focused on the speckles through the beam splitter via the reflective surface of the specimen. The target plate was illuminated by two LED lamps. The distance (Δ) between the mid-plane of the specimen and the target plate was ~70 mm. A Nikon D100 digital SLR camera fitted with a 70–300 mm lens and an adjustable bellows was placed in-front of the specimen at ~1200 mm (L). A small aperture ($F^{\#} = 11$) was selected for recording the speckles with a good focus. An 8-bit reference image was recorded with a resolution of 1504 × 1000 pixels in the no-load state. While loading, the images corresponding to the deformed state were recorded at a rate of 0.5 frames per second as the anticipated crack speed was low. The speckle images in the deformed state were correlated with the reference image using ARAMIS® image analysis software. For image correlation, a sub-image size of 35 × 35 pixels (scale factor = 35.08 μm/pixel) with 25 pixels of overlap was used to extract the local speckle displacements $\delta_{x;y}$ in the ROI. The

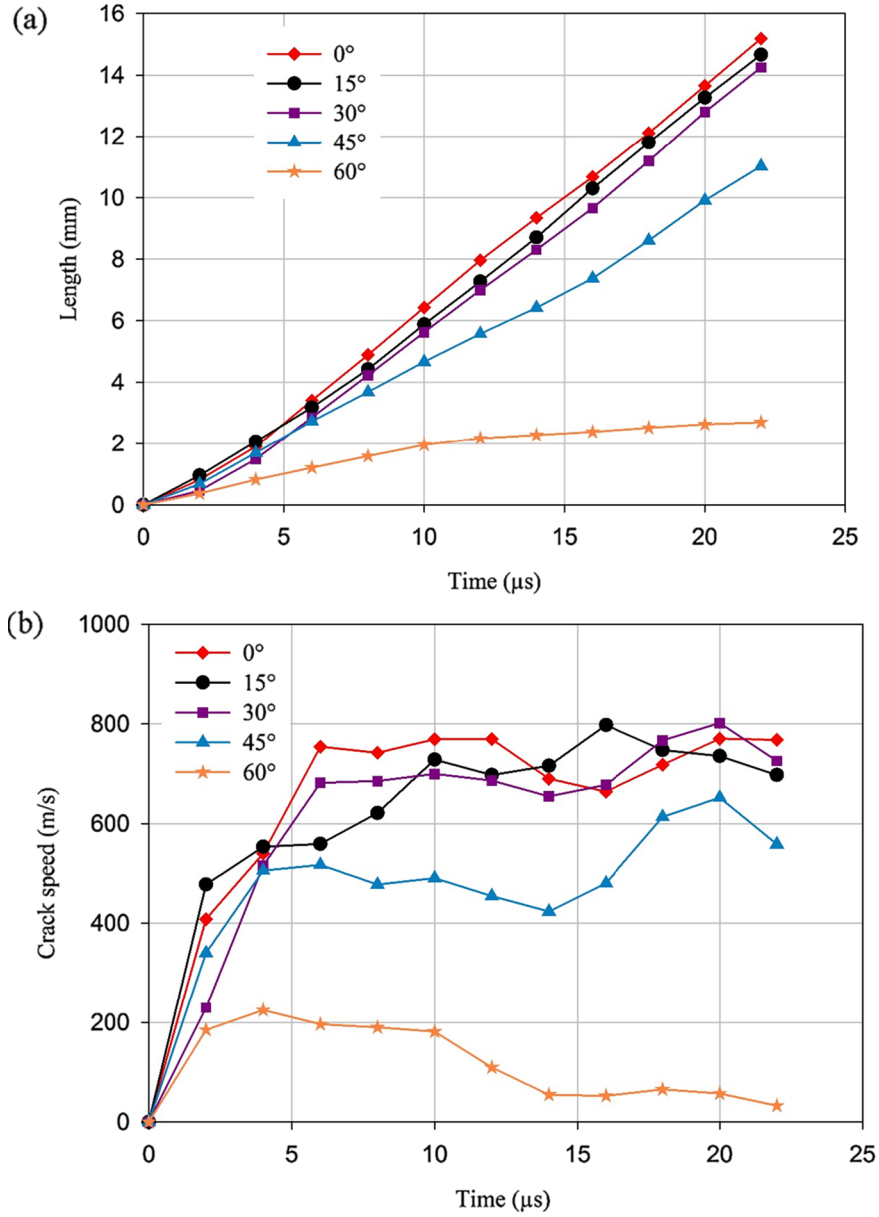

Fig. 9. Crack growth (a) and velocity (b) histories during dynamic fracture of CFRP with different fiber orientation.

displacement fields were then used to compute the two orthogonal surface slopes, $\frac{\partial w}{\partial x;y}$.

The measured surface slopes of $\frac{\partial w}{\partial x}$ around the crack-tip for $\alpha = 15^{\circ}$ are shown in Fig. 11 at a few select time instants. All the contours are plotted in the local crack-tip coordinates (x', y'); here the x'-axis is along the crack propagation direction and the y'-axis is normal to the crack. Unlike in the dynamic events which last a couple of hundred microseconds, the rigid body motions could occur during the static experiments as they last several minutes. The failure load histories for quasi-static fracture of CFRP are plotted as a function of the degree-of-anisotropy $\frac{E_{xx}}{E_{yy}}$ in Fig. 12(a). It includes two graphs, one for the load at crack initiation ($t = 0$) and the other for the critical/peak load. The complete failure occurred only after the specimens crossed the critical load. It can be observed that the load value after crack initiation for each CFRP coupon is lower than the corresponding critical/peak load. This is attributed to fiber bridging of the crack faces resulting in additional load bearing capacity in each coupon after crack initiation. This is evident in the load-displacement histories for all specimens, plotted in Fig. 12(b). An enlarged part of the plot for $\frac{E_{xx}}{E_{yy}} = 19$ (or $\alpha = 0^{\circ}$) is selected as an example to highlight crack initiation seen as a small kink in otherwise monotonic increase. In the inset, it can be observed that there is a small load drop, highlighted by the dotted circle, before the specimen attained the critical load, marked by the solid circle. The former represents the load at which the crack initiated first but continued to bear load until complete failure occurred after the

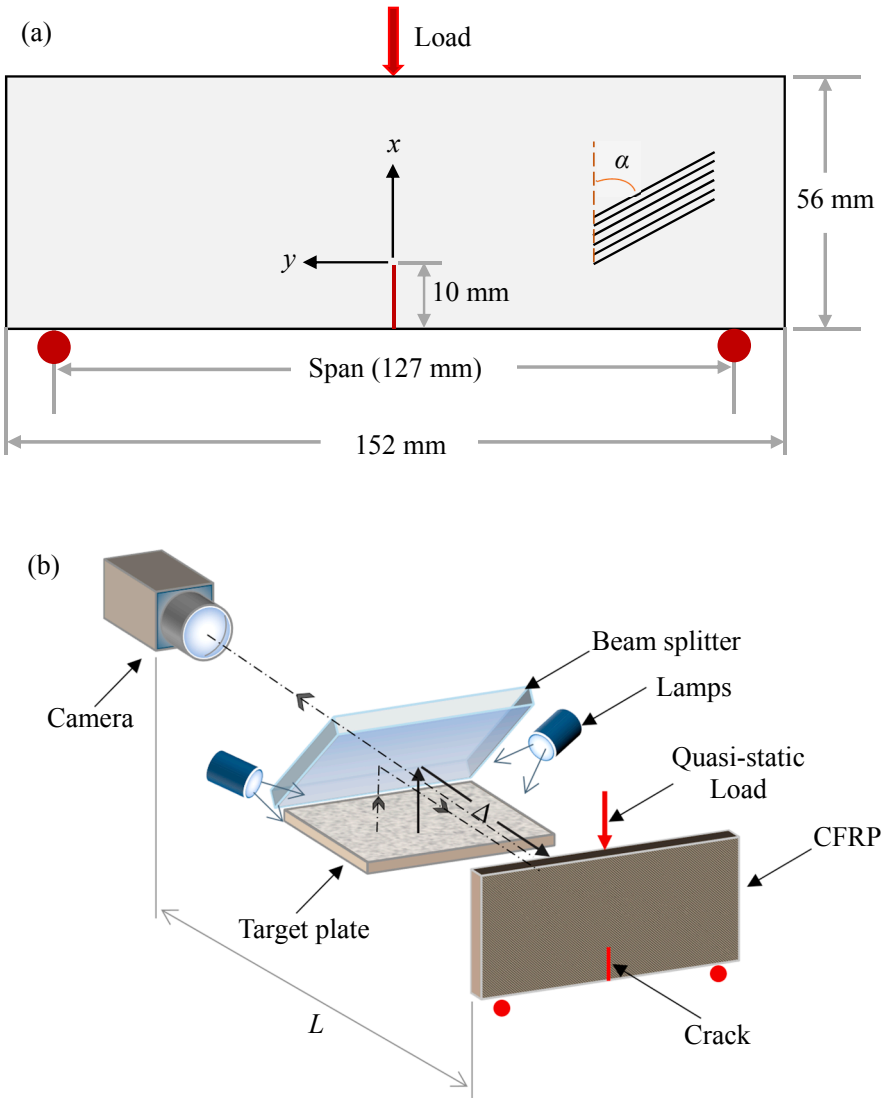

Fig. 10. Details of quasi-static fracture experiments: (a) Specimen configuration, (b) Schematic of experiment setup.

critical load was attained. Both the critical load and crack initiation load show similar decreasing trends with the degrees-of-anisotropy. *It should be noted that the crack growth was recorded for only 12 s, whereas the specimens took much longer to cross the critical load.*

5. Extraction of stress intensity factors (SIFs)

The measured DGS data in the local crack-tip coordinates (x', y') are used to extract the mode-I and -II stress intensity factors (SIFs). The corresponding surface slopes $\frac{\partial w}{\partial x';y'}$ are expressed in terms of $\frac{\partial w}{\partial x;y}$ in the global coordinates (x, y) using transformation equations,

$$\frac{\partial w}{\partial x'} = \frac{\partial w}{\partial x}\cos(\alpha) + \frac{\partial w}{\partial y}\sin(\alpha) \tag{2}$$

$$\frac{\partial w}{\partial y'} = -\frac{\partial w}{\partial x}\sin(\alpha) + \frac{\partial w}{\partial y}\cos(\alpha) \tag{3}$$

where α is the fiber orientation angle for each case. An example of these transformations is shown in Fig. 13. Fig. 13(a) (same as Fig. 7(g)) shows the measured surface slope $\frac{\partial w}{\partial x}$ in the global coordinate system (x, y) whereas the one in the local coordinate is shown in Fig. 13(b). The reorientation of the tri-lobed contours as a result of the transformation is readily evident.

Now, the measured surface slopes $\frac{\partial w}{\partial x';y'}$ for a dynamically growing mixed-mode crack are expressed as follows [15]:

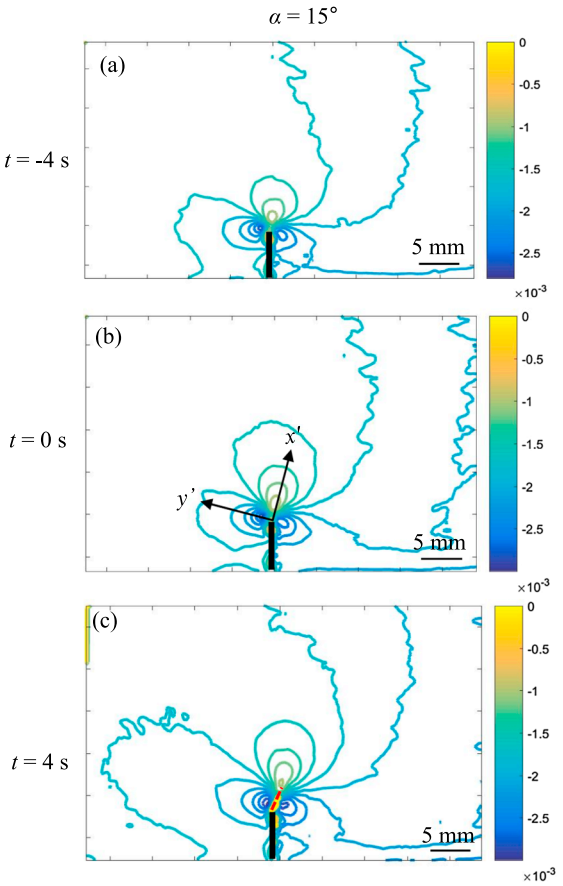

Fig. 11. Measured surface slopes of $\frac{\partial w}{\partial x}$ for quasi-static fracture tests on CFRP ($\alpha = 15^{\circ}$). Contour increments = 2×10^{-4} rad. (Black strips are overlaid to highlight the crack; broken red line suggests kinked crack path.) (For interpretation of the references to colour in this figure legend, the reader is referred to the web version of this article.)

$$\frac{\partial w}{\partial x'} = F_{11}(r, \theta)K_{\mathrm{I}} + F_{12}(r, \theta)K_{\mathrm{II}}$$
$$\frac{\partial w}{\partial y'} = F_{21}(r, \theta)K_{\mathrm{I}} + F_{22}(r, \theta)K_{\mathrm{II}} \tag{4}$$

where

$$F_{11} = -\frac{h}{4\sqrt{2\pi}R(v)}\,\mathrm{Re}\left\{\frac{\mu_2-\lambda_2}{\lambda_1-\lambda_2}\cdot\frac{\beta_1-\beta_2\mu_1\lambda_1}{(r\cos\theta+\mu_1 r\sin\theta)^{3/2}} - \frac{\mu_1-\lambda_1}{\lambda_1-\lambda_2}\cdot\frac{\beta_1-\beta_2\mu_2\lambda_2}{(r\cos\theta+\mu_2 r\sin\theta)^{3/2}}\right\}$$

$$F_{12} = \frac{h}{4\sqrt{2\pi}R(v)}\,\mathrm{Re}\left\{\frac{\gamma-\lambda\eta^2\mu_2\lambda_2}{\lambda_1-\lambda_2}\cdot\frac{\beta_1-\beta_2\mu_1\lambda_1}{(r\cos\theta+\mu_1 r\sin\theta)^{3/2}} - \frac{\gamma-\lambda\eta^2\mu_1\lambda_1}{\lambda_1-\lambda_2}\cdot\frac{\beta_1-\beta_2\mu_2\lambda_2}{(r\cos\theta+\mu_2 r\sin\theta)^{3/2}}\right\},$$

$$F_{21} = -\frac{h}{4\sqrt{2\pi}R(v)}\,\mathrm{Re}\left\{\frac{\mu_1(\mu_2-\lambda_2)}{\lambda_1-\lambda_2}\cdot\frac{\beta_1-\beta_2\mu_1\lambda_1}{(r\cos\theta+\mu_1 r\sin\theta)^{3/2}} - \frac{\mu_2(\mu_1-\lambda_1)}{\lambda_1-\lambda_2}\cdot\frac{\beta_1-\beta_2\mu_2\lambda_2}{(r\cos\theta+\mu_2 r\sin\theta)^{3/2}}\right\},$$

$$F_{22} = \frac{h}{4\sqrt{2\pi}R(v)}\,\mathrm{Re}\left\{\frac{\mu_1(\gamma-\lambda\eta^2\mu_2\lambda_2)}{\lambda_1-\lambda_2}\cdot\frac{\beta_1-\beta_2\mu_1\lambda_1}{(r\cos\theta+\mu_1 r\sin\theta)^{3/2}} - \frac{\mu_2(\gamma-\lambda\eta^2\mu_1\lambda_1)}{\lambda_1-\lambda_2}\cdot\frac{\beta_1-\beta_2\mu_2\lambda_2}{(r\cos\theta+\mu_2 r\sin\theta)^{3/2}}\right\},$$

h is the specimen thickness, (r, θ) denotes the crack-tip polar coordinates as shown in Fig. 13(b), and K_{I} and K_{II} are the dynamic stress intensity factors for mode-I and mode-II, respectively. The other parameters in Eq. (4) are defined as follows [15]:

$\beta_{1,2}$ are two material constants: $\beta_1 = s_{31}\eta^2 + s_{32}\gamma$; $\beta_2 = s_{31}\gamma + s_{32}\lambda\eta^2$; $R(v)$ is the generalized Rayleigh wave function: $R(v) = \sqrt{\lambda}\eta^2\alpha_l(v)\alpha_s(v) - \frac{\sqrt{\lambda}\eta^2\alpha_l(v)+\gamma^2\alpha_s(v)}{\sqrt{\lambda}\eta^2\alpha_l(v)+\alpha_s(v)}$;

$\lambda_i(v) = \frac{\eta^2\alpha_i^2(v)+\mu_i^2(v)}{(1+\gamma)\mu_i(v)}$, $i = 1, 2$;

μ_j $(j = 1, 2)$ are the two roots with positive imaginary part of the characteristic equation:

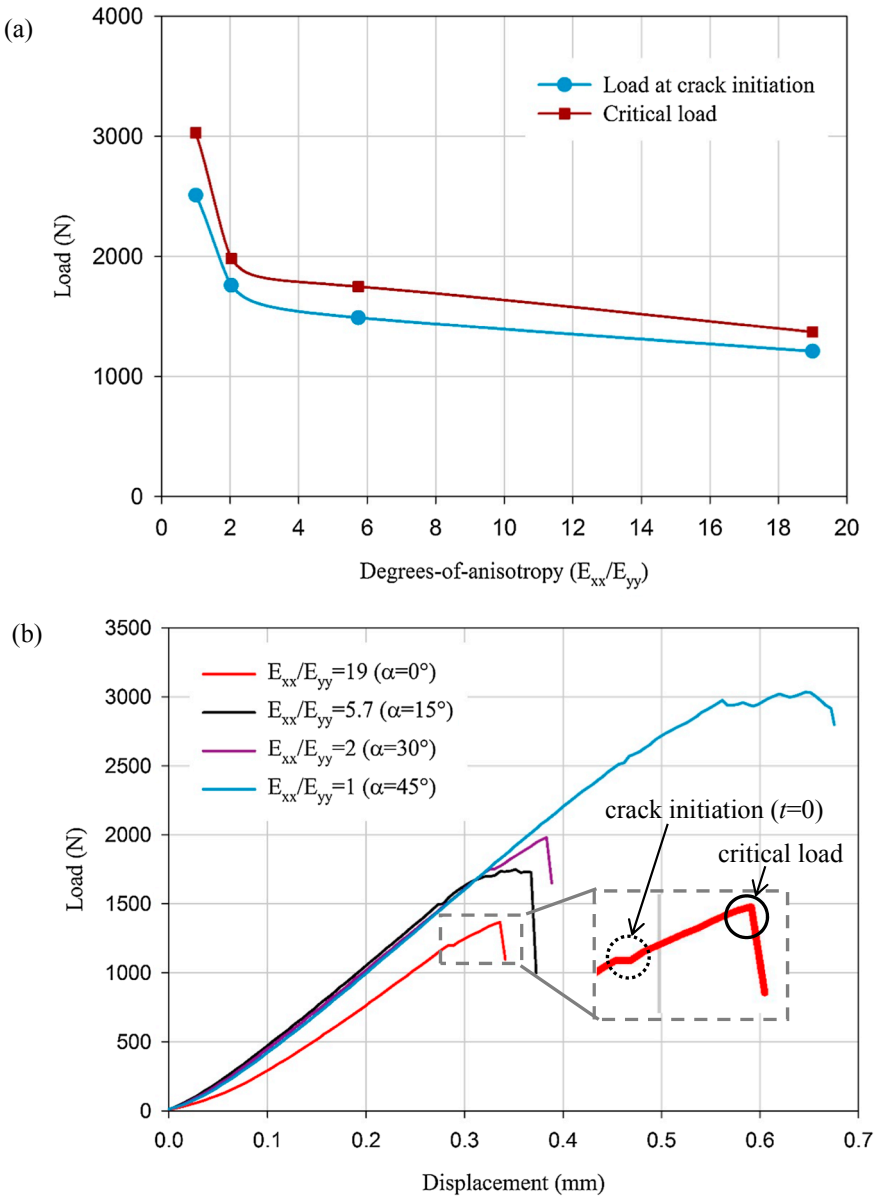

Fig. 12. (a) Fracture load variations for different fiber orientations, (b) Load vs. load-point deflection histories.

$$\mu^4 + \frac{\lambda\eta^4\alpha_l^2(v) + \alpha_s^2(v) - (1+\gamma)^2}{\lambda\eta^2}\mu^2 + \frac{\alpha_l^2(v)\alpha_s^2(v)}{\lambda} = 0;$$

$\lambda = \frac{s_{11}}{s_{22}}$, $\rho = \frac{2s_{12}+s_{66}}{2\sqrt{s_{11}s_{22}}}$, $\kappa = \frac{3\sqrt{s_{11}s_{22}}+s_{12}}{\sqrt{s_{11}s_{22}}-s_{12}}$, $c_l = \left(\frac{c_{11}}{d}\right)^{1/2}$, $c_s = \left(\frac{c_{66}}{d}\right)^{1/2}$, $\alpha_l^2(v) = 1 - \frac{v^2}{c_l^2}$, $\alpha_s^2(v) = 1 - \frac{v^2}{c_s^2}$, $\eta^2 = \left(\frac{c_l}{c_s}\right)^2$, $\gamma = \sqrt{\lambda}\eta^2\left(\frac{3-\kappa}{1+\kappa}\right)$, in which c_l is the longitudinal wave speed, c_s is the shear wave speed, s_{ij} ($i, j = 1,\ldots,6$) are the elements of the compliance matrix, c_{ij} ($i, j = 1,\ldots,6$) are the elements of stiffness matrix, d is mass density, v is the crack-tip velocity.

As noted earlier, rigid body motions could occur during experiments in general, and quasi-static conditions in particular. These can be tackled by enforcing symmetry and far-field boundary conditions [27,28] involving mode-I crack problems or by including rigid body motion terms while extracting the fracture parameters. That is, Eq. (4) can be modified as,

$$\frac{\partial w}{\partial x'} = F_{11}(r,\theta)K_{\mathrm{I}} + F_{12}(r,\theta)K_{\mathrm{II}} + C_1x' + C_2y' + C_3$$

$$\frac{\partial w}{\partial y'} = F_{21}(r,\theta)K_{\mathrm{I}} + F_{22}(r,\theta)K_{\mathrm{II}} + D_1x' + D_2y' + D_3$$

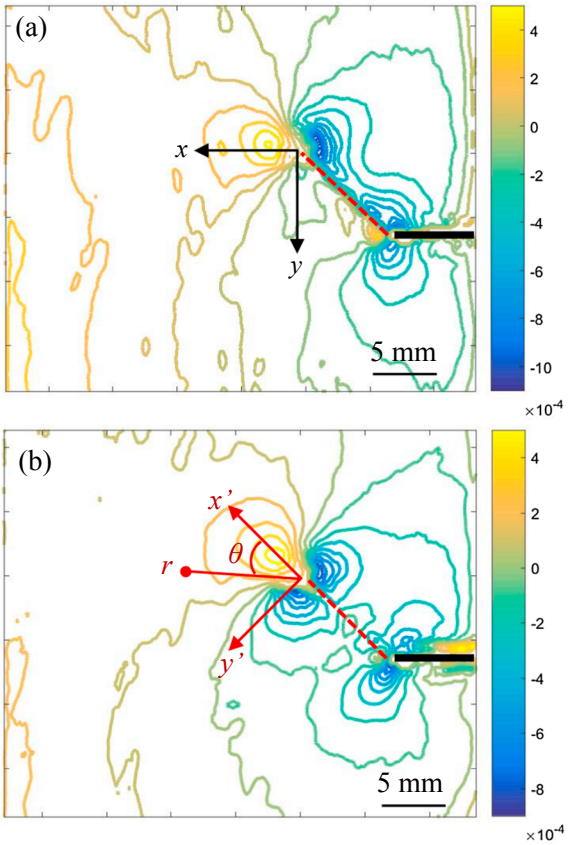

Fig. 13. Measured surface slopes for α = 45° in (a) $\frac{\partial w}{\partial x}$ contours, (b) $\frac{\partial w}{\partial x'}$ contours. (Black strip highlights the crack; broken red line suggests kinked crack path.) (For interpretation of the references to colour in this figure legend, the reader is referred to the web version of this article.)

where the bilinear terms with unknown coefficients $C_1 - C_3$ and $D_1 - D_3$ account for rigid translations and rotations.

In the analysis, $\frac{\partial w}{\partial x'}$ data in the region $0.5 \le r/h \le 1.5$ and angular extent of $-140^\circ \le \theta \le 140^\circ$ near the crack-tip were used to calculate SIFs. The choice of the region excluded triaxial deformations, further lessening the impact of crack-tip location errors on the estimated stress intensity factors. (It should be noted that least-squares over-deterministic SIF extraction showed that coefficients for the rigid rotation terms were significantly smaller, typically two orders of magnitude, relative to the constant term). Recognizing that the above equations degenerate to the quasi-static counterparts in the limit the crack-tip velocity, v, approaches zero, the equations were utilized in the case of both statically and dynamically loaded stationary crack experiments.

Next, the SIFs were used to evaluate the strain energy release rate, G [15] as,

$$G = \frac{\eta}{2c_{66}R(v)}\left[1 - \left(\frac{1+\gamma}{\sqrt{\lambda}\eta^2\alpha_l(v) + \alpha_s(v)}\right)^2\right]^{1/2}\left[\alpha_l(v)K_I^2 + \sqrt{\lambda}\alpha_s(v)K_{II}^2\right] \tag{5}$$

for a moving crack in dynamic fracture case. Further, Eq. (5) can be reduced to

$$G = s_{11}\sqrt{\frac{1+\rho}{2}}\left(\lambda^{-3/4}K_I^2 + \lambda^{-1/4}K_{II}^2\right) \tag{6}$$

for a dynamically loaded stationary crack and quasi-static crack cases.

6. Results and discussion

A compilation of mode-I and mode-II stress intensity factor histories evaluated from r-DGS measurements for dynamically fractured CFRP specimens for different fiber orientations are plotted in Fig. 14(a). The time axis of each plot was independently shifted so that $t = 0$ μs corresponds to crack initiation at the original notch-tip as determined from the optically generated contours. The solid and open symbols in Fig. 14(a) represent K_I and K_{II}, respectively. The K_I histories in all cases increase monotonically prior to crack initiation but drop abruptly once crack initiation occurs. Following the drop, they attain different but nearly steady values during crack propagation period, plotted up to 22 μs after initiation. As expected, nominally mode-I fracture occurs in $\alpha = 0^\circ$case as K_{II} values oscillate close to zero in the pre- and post-initiation regimes. When mixed-mode fractures occur in other CFRP specimens

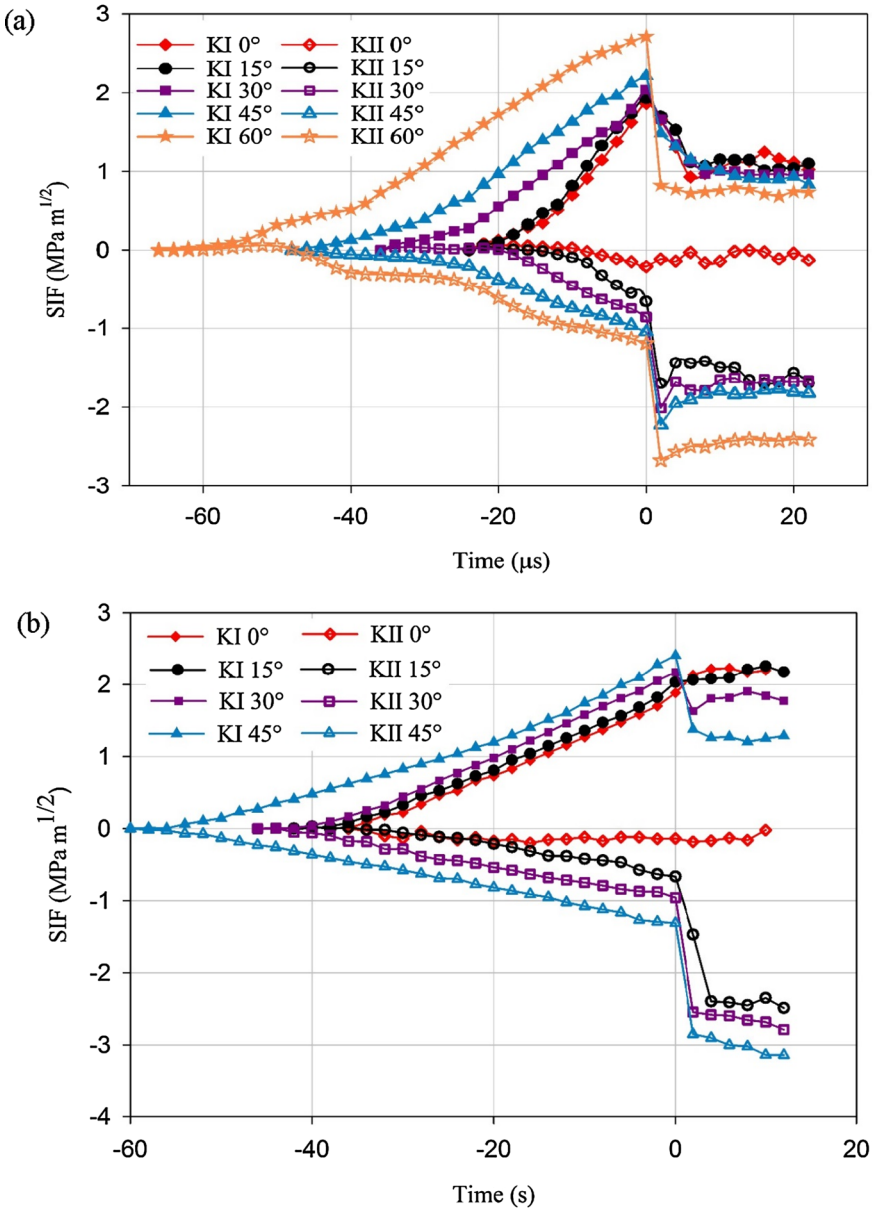

Fig. 14. Compilation of measured stress intensity factor (SIF) histories for CFRP subjected to (a) dynamic loading and (b) quasi-static loading. ($t = 0$ corresponds to apparent crack initiation.)

with fiber orientation $\alpha = 15$–60°, the K_{II} values increase in magnitude before crack initiation and further increase abruptly after crack initiation before settling to different but relatively steady values in the crack propagation period. It can be further observed that, with the increase of fiber orientation angle α, there is an increase in the magnitude of K_{II} at crack initiation with larger α resulting in higher plateau value. Additionally, as evident from the plot, it took longer for the crack to initiate with increasing fiber orientation angle; for example, it took approx. 50 μs for $\alpha = 45^{\circ}$ whereas it was around ~25 μs for $\alpha = 15^{\circ}$. (It should be noted here that the post-initiation variations of stress intensity factors, particularly the K_{II} histories reported here deviate from the ones in Ref. [22]. This is attributed to multiple differences in experimental details including loading apparatus and hence the loading profiles (drop-tower vs. Hopkinson bar), nature of the recording devise (multi-sensor vs. single sensor ultrahigh-speed camera), temporal resolution used (250 vs. 500 Kfps), and uncertainty associated with the crack tip location (non-singular displacements in DIC vs. singular surface slopes in r-DGS).

A similar compilation of the two stress intensity factor histories for all configurations of quasi-static fracture of CFRP are plotted in Fig. 14(b). Again, the time axes of the plots were shifted independently so that $t = 0$ corresponds to crack initiation at the original notch-tip, determined from the optical contours. As noted earlier, the load to initiate the crack in the specimen with $\alpha = 60^{\circ}$ exceeded

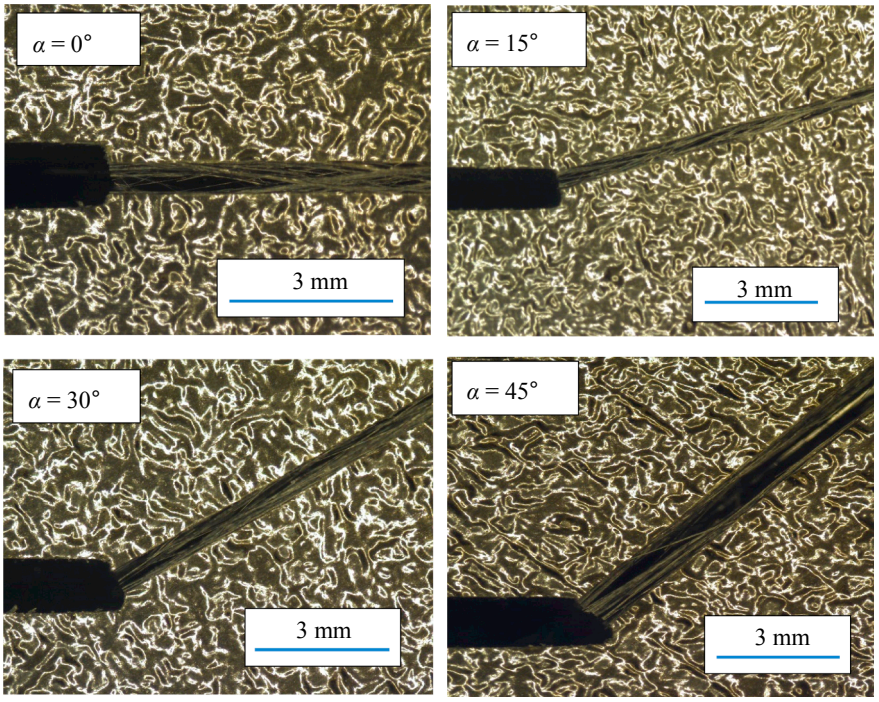

Fig. 15. Cracked faces bridged by fibers in quasi-static experiments. (The random pattern elsewhere is due to the surface texture and angular illumination).

the limit of the testing machine and hence was not studied. The K_I and K_{II} histories with $\alpha = 30^\circ$ and 45° subjected to quasi-static loading have trends quite similar to the dynamic counterparts. That is, the optically extracted K_I and K_{II} values increase monotonically and somewhat linearly up to crack initiation. The K_I values abruptly drop at crack initiation before reaching a plateau. The K_I histories for $\alpha = 0^\circ$ and 15°, however, show a slightly different trend after crack initiation. A change in the slope of K_I variation but without an abrupt drop is evident. This is attributed to fibers bridging the crack flanks preventing a significant drop from occurring in the K_I values at crack initiation in these two cases. These crack bridges are evident from the micrographs of the failed samples shown in Fig. 15. That is, fiber bridges in $\alpha = 0^\circ$ and 15° cases contribute to a higher percentage of overall crack growth resistance when compared to $\alpha = 30^\circ$ and 45° cases as load at crack initiation for the former two cases are much smaller than those for the latter ones (see, Fig. 12(a)). The magnitude of K_{II} values in all cases (except $\alpha = 0^\circ$) increase monotonically up to crack initiation. Furthermore, as in the dynamic cases, the crack initiation event in these cases is accompanied by an abrupt increase in the magnitude of K_{II} followed by the values reach different plateaus similar to the K_I histories. Also, these plateau values of K_{II} increase with increasing fiber orientation.

The energy release rate, G, histories were determined from Eqs. (5) and (6) for both high- and low-rate loading conditions and the results are compiled in Fig. 16. In the pre-initiation regime, the G histories monotonically increase up to crack initiation with higher fiber orientation producing higher values at initiation. In the dynamic loading cases (Fig. 16(a)), the peak value of G (340–590 N/m; see Table 3) occurred either at $t = 0$ or one time step (2 μs) after that, possibly due to the fiber bridging effects noted earlier. Aside this, the G values drop in all dynamic fracture cases after crack initiation and show a tendency to attain separate plateau values in different cases. The plateau values for different fiber orientations vary between ~145 N/m in $\alpha = 0^\circ$ to ~300 N/m in $\alpha = 45^\circ$, nearly one half of the (peak) values at crack initiation. In the quasi-static loading cases (Fig. 16(b)), the values of G show noticeably different trend in the post-initiation regime although they increase monotonically up to crack initiation for all fiber orientations as in the dynamic cases. Again, the values of G corresponding to crack initiation increases with fiber angle and are higher than the corresponding dynamic counterparts (Table 3). A striking difference in the quasi-static G histories is in the post-initiation regime where (i) a significant increase in G values are seen following crack initiation and, (ii) the G values continue to increase, though at a reduced rate, during the window-of-observation suggesting a relatively graceful failure prior to rapid fracture. This difference relative to the dynamic counterpart is significant as it conveys an important loading rate dependent post-initiation behavior of this CFRP namely stress wave loading produced a weaker post-initiation response relative to the quasi-static counterparts.

A compilation of data for energy release rate, G, mode-mixity, ψ $(= \tan^{-1}\left(\frac{K_{II}}{K_I}\right))$, and time rate of change of effective SIF, $\frac{dK_{eff}}{dt}$ or $\dot{K}_{eff}$ $(K_{eff} = \sqrt{K_I^2 + K_{II}^2})$, are summarized in Table 3. The $\dot{K}_{eff}$ for the dynamic experiments are in the 6×10^4 to 12×10^4 MPa√m•s^{-1} range whereas they are 6×10^{-2} MPa√m•s^{-1} for static conditions. The values of G and ψ during crack growth are averaged from 8 μs to 22 μs and from 4 s to 12 s in dynamic and quasi-static cases, respectively. These values increase with fiber orientation in case of both the loading rates. It can be observed that energy release rates under quasi-static conditions during crack growth are higher than

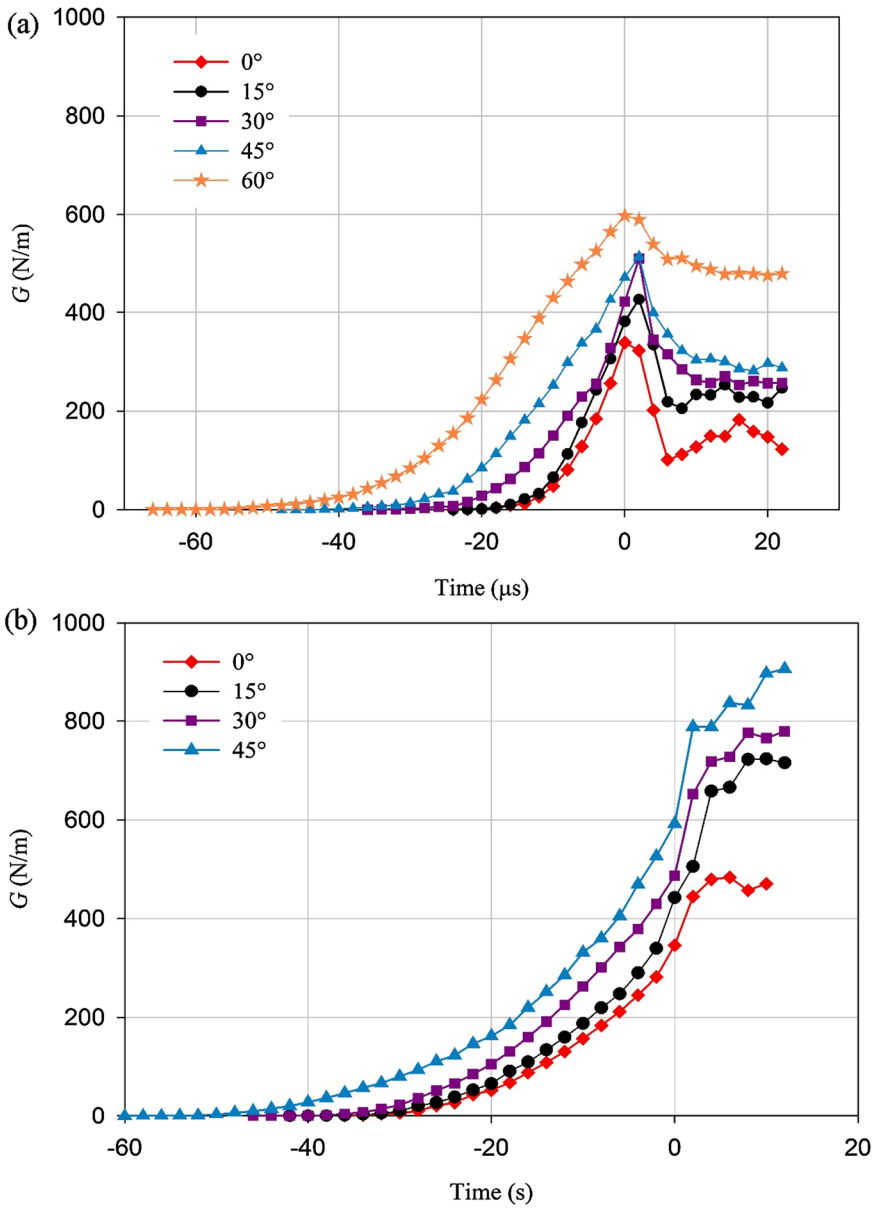

Fig. 16. Energy release rate histories for CFRP with different fiber orientations (a) dynamic fracture and (b) quasi-static fracture. (t = 0 corresponds to crack initiation.)

Table 3
Compilation of energy release rate (G), mode-mixity (ψ) and time rate of change of effective SIF ($\dot{K}_{eff}$).

	E_{xx}/E_{yy}	19	5.7	2	1	0.5
Dynamic	G_initiation (N/m)	339	382	423	473	598
	G_growth (N/m)	144 ± 22	231 ± 15	263 ± 10	298 ± 13	487 ± 11
	ψ_initiation (deg.)	−6	−18	−23	−25	−24
	ψ_growth (deg.)	−4 ± 3	−55 ± 2	−60 ± 1	−63 ± 2	−73 ± 1
	$\dot{K}_{eff}$ (MPa $m^{1/2}$/s)	12×10^4	12×10^4	8×10^4	6×10^4	6×10^4
Quasi-static	G_initiation (N/m)	346	443	487	592	–
	G_growth (N/m)	473 ± 11	697 ± 32	754 ± 28	853 ± 50	–
	ψ_initiation (deg.)	−4	−18	−23	−29	–
	$\dot{K}_{eff}$ (MPa $m^{1/2}$/s)	6×10^{-2}	6×10^{-2}	6×10^{-2}	6×10^{-2}	–

the corresponding values under dynamic loading conditions suggesting a weaker post-initiation response relative to the quasi-static counterparts.

In the context of the above discussion, it is worth recapping the results of some reports in the literature. Tang et al. [4] investigated fracture mechanism of three-dimensional CFRP under static and dynamic loadings, and reported that cracks propagated in a zigzag pattern during static loading condition, whereas a region of surface ablation occurred seen under dynamic loading conditions. Lee et al. [22] studied fracture behavior of unidirectional CFRP under static and dynamic loadings, and reported that fiber bridging in quasi-static loading condition. Mallon et al. [25] studied fracture behavior of orthotropic woven glass fiber-reinforced composites under quasi-static and shock loading conditions. Fiber bridging was observed during quasi-static loading, and was associated with higher stress intensity factors. Hoffmann et al. [26] reported that the strain-energy release rate of a composite laminate under high-rate loading was lower than its quasi-static counterpart. They also observed a more extensive damage zone under quasi-static conditions than high-rate loading counterparts.

7. Conclusions

Static and dynamic fracture behaviors of unidirectional CFRP laminates made of T800s/3900-2 are studied. Single edge notched coupons subjected to geometrically symmetric loading – quasi-static three-point bending and single-point dynamic impact – are investigated. The effect of fiber orientation on crack initiation and growth are examined at two distinct loading rates, 10^4 MPa$\sqrt{\text{m}}\cdot\text{s}^{-1}$ and 10^{-2} MPa$\sqrt{\text{m}}\cdot\text{s}^{-1}$, characterized by the rate of change of stress intensity factors at crack initiation. A vision-based full-field optical method called reflection-mode Digital Gradient Sensing or r-DGS is also extended to study fracture behavior and evaluate the fracture parameters in fiber reinforced plastics. For conducting dynamic measurements, r-DGS is implemented with an ultrahigh-speed single sensor camera. The measured optical fields physically represent small angular deflections of light rays in the 10^{-5}–10^{-3} rad range which are related to two orthogonal surface slopes in the ROI that are singular at the crack-tip. Besides visualizing the full-field deformations, the optical measurements are used in concurrence with elasto-static and elasto-dynamic crack-tip fields for orthotropic materials to quantify stress intensity factors, energy release rates, loading rates and crack speeds. Based on the measurements, the following observations are made:

- The inclined fiber orientation relative to the crack direction have forced the crack-tip deformations and crack growth to occur under mixed-mode conditions in geometrically symmetric loading configurations. That is, mixed-mode crack growth ensued along the fibers in all non-zero fiber orientation cases. A wide range of speeds, from 800 m/s in the $\alpha = 0^\circ$ case to less than 200 m/s when $\alpha = 60^\circ$, under dynamic impact loading conditions occurred.
- Under quasi-static loading conditions, crack initiation occurred at a load that continued to increase until a peak/critical load was reached. This is due to the formation of fiber bridges across the crack flanks. Both crack initiation load and critical loads decrease with the degree-of-anisotropy defined as E_{xx}/E_{yy}.
- A monotonic increase in both mode-I and -II stress intensity factors occurred until crack initiation. The crack-tip loading rates in the dynamic cases were of the order of 10^4 MPa$\sqrt{\text{m}}\cdot\text{s}^{-1}$ whereas they were six orders of magnitude lower in the quasi-static counterparts.
- The crack initiation events in the dynamic cases were accompanied by an abrupt drop in K_{I} whereas an abrupt increase in K_{II} magnitude in all non-zero fiber angles. In the quasi-static cases, however, the latter was true in all non-zero fiber angles whereas the former was true for angles 30° and 45° cases as fiber bridges strongly influenced post-initiation behavior in the 0° and 15° cases. It consistently took longer for the crack to initiate when the fiber angles were larger.
- The energy release rate (G) variations show monotonic increase until crack initiation in both quasi-static and dynamic conditions. The post-initiation characteristics, however, are quite different. An abrupt drop in G followed by steady values during the observation window in the dynamic cases contrast with increasing trends in the static cases. A weaker post-initiation crack growth could cause sudden failure under dynamic conditions whereas static loading could result in a more graceful failure.
- Apart from the zero-degree fiber orientation case, energy release rate when the crack initiates under dynamic mixed-mode conditions is lower than the corresponding quasi-static cases. During growth, however, the energy release rates are approx. one-half that at crack initiation in dynamic loading conditions.

Acknowledgments

Partial support of this research from the U.S. Army grants W31P4Q-14-C-0049, W911NF-16-1-0093 and W911NF-15-1-0357 (DURIP) are gratefully acknowledged. The authors are also grateful to Dr. Dongyeon Lee, Toray Composite Materials America, Inc., for providing the CFRP laminates studied in this work.

References

[1] Ye L, Lu Y, Su Z, Meng G. Functionalized composite structures for new generation airframes: a review. Compos Sci Technol 2005;65:1436–46.
[2] Williams G, Trask R, Bond I. A self-healing carbon fibre reinforced polymer for aerospace applications. Compos A 2007;38:1525–32.
[3] Gibson RF. A review of recent research on mechanics of multifunctional composite materials and structures. Compos Struct 2010;92:2793–810.
[4] Tang G, Yan Y, Chen X, Zhang J, Xu B, Feng Z. Dynamic damage and fracture mechanism of three-dimensional braided carbon fiber/epoxy resin composites. Mater Des 2001;22:21–5.
[5] Liu Q, Hughes M. The fracture behaviour and toughness of woven flax fibre reinforced epoxy composites. Compos A 2008;39:1644–52.

[6] Arai M, Noro Y, Sugimoto K-I, Endo M. Mode I and mode II interlaminar fracture toughness of CFRP laminates toughened by carbon nanofiber interlayer. Compos Sci Technol 2008;68:516–25.
[7] May M. Measuring the rate-dependent mode I fracture toughness of composites – a review. Compos A 2016;81:1–12.
[8] Beckermann GW, Pickering KL. Mode I and Mode II interlaminar fracture toughness of composite laminates interleaved with electrospun nanofibre veils. Compos A 2015;72:11–21.
[9] Seyhan AT, Tanoglu M, Schulte K. Mode I and mode II fracture toughness of E-glass non-crimp fabric/carbon nanotube (CNT) modified polymer based composites. Eng Fract Mech 2008;75:5151–62.
[10] Shukla A, Agarwal B, Bhushan B. Determination of stress intensity factor in orthotropic composite materials using strain gages. Eng Fract Mech 1989;32:469–77.
[11] Khanna S, Shukla A. On the use of strain gages in dynamic fracture mechanics. Eng Fract Mech 1995;51:933–48.
[12] Freire JLF, Antonelli RA, Dror Y, Voloshin AS. Application of reflection orthotropic photoelasticity to laminated composites. J Compos Mater 1989;23:42–57.
[13] Shukla A, Khanna SK. Effect of fiber reinforcement on dynamic crack growth in brittle matrix composites. J Eng Mater Technol 1993;115:140–5.
[14] Tippur HV, Krishnaswamy S, Rosakis AJ. Optical mapping of crack tip deformations using the methods of transmission and reflection coherent gradient sensing: a study of crack tip K-dominance. Int J Fract 1991;52:91–117.
[15] Liu C, Rosakis AJ, Stout MG. Dynamic fracture toughness of a unidirectional graphite/epoxy composite. Proceedings of the symposium on “dynamic effects in composite structures”, IMECE 2001, New York. 2001.
[16] Liu C, Rosakis AJ, Ellis RW, Stout MG. A study of the fracture behavior of unindirectional fiber- reinforced composite using coherent gradient sensing (CGS) interferometry. Int J Fract 1998;90:355–82.
[17] Hatta H, Aly-Hassan MS, Hatsukade Y, Wakayama S, Suemasu H, Kasai N. Damage detection of C/C composites using ESPI and SQUID techniques. Compos Sci Technol 2005;65:1098–106.
[18] Pan B, Qian K, Xie H, Asundi A. Two-dimensional digital image correlation for in-plane displacement and strain measurement: a review. Meas Sci Technol 2009;20:062001.
[19] Mekky W, Nicholson PS. The fracture toughness of Ni/Al2O3 laminates by digital image correlation I: experimental crack opening displacement and R-curves. Eng Fract Mech 2006;73:571–82.
[20] Kirugulige MS, Tippur HV. Measurement of fracture parameters for a mixed-mode crack driven by stress waves using image correlation technique and high-speed digital photography. Strain 2009;45:108–22.
[21] Kirugulige MS, Tippur HV, Denney TS. Measurement of transient deformations using digital image correlation method and high-speed photography: application to dynamic fracture. Appl Opt 2007;46(22):5083–96.
[22] Lee D, Tippur H, Bogert P. Quasi-static and dynamic fracture of graphite/epoxy composites: an optical study of loading-rate effects. Compos B 2010;41:462–74.
[23] Lee D, Tippur H, Kirugulige M. Experimental study of dynamic crack growth in unidirectional graphite/epoxy composites using digital image correlation method and high-speed photography. J Compos Mater 2009;43:2081–108.
[24] Bedsole RW, Bogert PB, Tippur HV. An experimental investigation of interlaminar and intralaminar dynamic fracture of CFRPs: effect of matrix modification using carbon nanotubes. Compos Struct 2015;132:1043–55.
[25] Mallon S, Koohbor B, Kidane A, Sutton MA. Fracture behavior of prestressed composites subjected to shock loading: a DIC-based study. Exp Mech 2015;55:211–25.
[26] Hoffmann J, Cui H, Petrinic N. Determination of the strain-energy release rate of a composite laminate under high-rate tensile deformation in fibre direction. Compos Sci Technol 2018;164:110–9.
[27] Periasamy C, Tippur HV. Full-field digital gradient sensing method for evaluating stress gradients in transparent solids. Appl Opt 2012;51(12):2088–97.
[28] Periasamy C, Tippur HV. A full-field reflection-mode digital gradient sensing method for measuring orthogonal slopes and curvatures of thin structures. Meas Sci Technol 2013;24:025202.
[29] Miao C, Sundaram BM, Huang L, Tippur HV. Surface profile and stress field evaluation using digital gradient sensing method. Meas Sci Technol 2016;27:095203.
[30] Miao C, Tippur HV. Measurement of sub-micron deformations and stresses at microsecond intervals in laterally impacted composite plates using digital gradient sensing. J Dyn Behav Mater 2018:1–23. https://doi.org/10.1007/s40870-018-0156-4.
[31] Miao C, Tippur HV. Higher sensitivity Digital Gradient Sensing configurations for quantitative visualization of stress gradients in transparent solids. Opt Lasers Eng 2018;108:54–67.
[32] Sundaram BM, Tippur HV. Dynamics of crack penetration vs. branching at a weak interface: an experimental study. J Mech Phys Solids 2016;96:312–32.
[33] Sundaram BM, Tippur HV. Dynamic fracture of soda-lime glass: a full-field optical investigation of crack initiation, propagation and branching. J Mech Phys Solids 2018. https://doi.org/10.1016/j.jmps.2018.04.010.
[34] Sundaram BM, Tippur HV. Full-field measurement of contact-point and crack-tip deformations in soda-lime glass. Part-II: stress wave loading. Int J Appl Glass Sci 2018;9:123–36.
[35] Tippur HV. Optical techniques in dynamic fracture mechanics. Dynamic fracture mechanics. World Scientific Publications; 2006.
[36] Tran T, Simkins D, Lim SH, Kelly D, Pearce G, Prusty GB, et al. Application of a scalar strain-based damage onset theory to the failure of a complex composite specimen. 28th International Congress of the Aeronautical Science, Brisbane, Australia. 2012.
[37] Jajam KC, Tippur HV. Quasi-static and dynamic fracture behavior of particulate polymer composites: a study of nano- vs. micro-size filler and loading-rate effects. Compos B 2012;43:3467–81.